

Deriving shallow-water sediment properties using post-stack acoustic impedance inversion

Mark E. Vardy

School of Ocean and Earth Sciences, National Oceanography Centre, European Way, Southampton, SO14 3ZH, UK

Received April 2014, revision accepted October 2014

ABSTRACT

In contrast to the use of marine seismic reflection techniques for reservoir-scale applications, where seismic inversion for quantitative sediment analysis is common, shallow-water, very-high-resolution seismic reflection data are seldom used for more than qualitative reflection interpretation. Here, a quantitative analysis of very-high-resolution marine seismic reflection profiles from a shallow-water (<50 m water depth) fjord in northern Norway is presented. Acquired using Sparker, Boomer, and Chirp sources, the failure plane of multiple local landslides correlates with a composite reflection that reverses polarity to the south. Using a genetic algorithm, a 1D post-stack acoustic impedance inversion of all three profiles is performed, calibrating against multi-sensor core logger (MSCL) data from cores. Using empirical relationships the resulting impedance profiles are related to remote sediment properties, including: P-wave velocity; density; mean grain size; and porosity. The composite reflector is consistently identified by all three data sources as a finer-grained (by one ϕ), lower density (c. 0.2 g/cm³ less than background) thin bed, with an anomalous low velocity zone (at least 100 m/s lower than background) associated with the polarity reversal to the south. Such a velocity contrast is consistent with an accumulation of shallow free gas trapped within the finer-grain, less permeable layer. This study represents the first application of acoustic impedance inversion to very-high-resolution seismic reflection data and demonstrates the potential for directly relating seismic reflection data with sediment properties using a variety of commonly used shallow seismic profiling sources.

INTRODUCTION

Very-high-resolution seismic reflection profiling using Sparker, Boomer and Chirp sources is commonly used for marine engineering (e.g., Schock *et al.* 2001), archaeology (e.g., Plets *et al.* 2008), homeland defence (e.g., Vardy *et al.* 2008), and geological applications (e.g., Stoker *et al.* 2009). Traditional seismic reflection processing and interpretation techniques focus on the architecture of the reflections, which originate at stratigraphic interfaces in the subsurface. Although the amplitude and polarity of these reflections can provide some information about the stratigraphic units forming these interfaces, this approach is predominantly limited to providing information about the subsurface structure. There are some methods to extract more quantitative reflection coefficient and/or acoustic quality factor (Q_p) information (e.g. Schock *et al.* 1989; Panda *et al.* 1994; Bull *et al.* 1998; Stevenson *et al.* 2002; Pinson *et al.* 2008, 2013), but for most surveys, information about the nature of the sediments comes from direct sampling through coring and/or cone penetrometer (CPTU) testing (e.g., Stoker *et al.* 2009; Vanneste *et al.* 2012).

In spatially heterogeneous areas, where a large number of cores/CPTUs are required, direct sampling can quickly become time consuming and expensive. This is compounded by unsolved issues regarding the preservation of certain key soil properties (e.g., porosity) during sampling. Over the last few decades, the petroleum industry has solved these issues by developing inversion techniques to generate acoustic or acoustic/elastic models of the subsurface from seismic reflection data. Cast as either pre-stack full waveform inversion (producing a model of P- and S-wave velocity, density, and attenuation) or post-stack impedance inversion (producing an impedance model), these techniques are now widely used for reservoir characterisation and monitoring (e.g., Mallick 2001; Bosch *et al.* 2010; Wagner *et al.* 2012) and are beginning to see use for basin-scale academic applications (Morgan *et al.* 2011, 2013).

In this study, I present the first application of acoustic impedance inversion to very-high-resolution marine seismic reflection data. A genetic algorithm (Goldberg 1989) is applied to Sparker, Boomer, and Chirp profiles, and the resulting impedance profiles related to sediment properties through empirical relationships. The results demonstrate a strong correlation with direct sampling, indicating the potential of impedance inversion for

* mev@noc.soton.ac.uk

3 remotely characterising shallow-water, nearshore sediments.
 4 Such methods permit soil properties to be spatially mapped at a
 5 high lateral resolution (metre-scale) over large areas quickly and
 6 efficiently, reducing the need for extensive and expensive coring
 7 campaigns. The implications for marine geohazard assessment
 8 are particularly significant, as these methods allow *in situ* soil
 9 properties to be mapped at a spatial resolution not possible by
 10 direct sampling.

11 INVERSION APPROACH

12 Forward Model

13 This paper deals specifically with shallow-water seismic reflection
 14 data (termed very-high-resolution hereafter; Wardell *et al.*
 15 2002), which is of sub-metre resolution and is commonly
 16 acquired using Sparker, Boomer and Chirp sources. In contrast
 17 to typical petroleum industry data, very-high-resolution seismic
 18 reflection acquisition methods are often technologically limited.
 19 Multi-offset data are rare, even in the 2D case (e.g., Palamenghi
 20 *et al.* 2011; Pinson *et al.* 2013), while there are only a handful of
 21 very-high-resolution 3D data examples (Gutowski *et al.* 2008;
 22 Plets *et al.* 2008; Vardy *et al.* 2008, 2010, 2012; Muller *et al.*
 23 2009; Mueller *et al.* 2013). This lack of significant source-
 24 receiver offsets allows the inversion process to be simplified,
 25 considering only the normal incident, plane-wave case in the
 26 classical manner of Cooke and Schneider (1983) and Oldenburg
 27 *et al.* (1983). In doing so, the seismic trace is cast as a 1-D con-
 28 volution between the Earth's reflectivity series and the seismic
 29 wavelet and is treated as a purely acoustic problem. No attempt
 30 is made to accommodate mode conversion and the elastic case.
 31

32 In this instance, the forward modelling case is straightfor-
 33 ward. The reflectivity series is easily calculated for each impedance
 34 model using the standard reflection coefficient equation
 35 (Sheriff 2002):

$$36 \quad R_i(m) = \frac{Z_{i-1} - Z_i}{Z_{i-1} + Z_i} \quad (1)$$

37 where $R_i(m)$ is the reflection coefficient for model m at time i ,
 38 and Z_i is the acoustic impedance at time i .

39 The associated synthetic trace can then be calculated through
 40 convolution of this reflectivity series with a suitable source
 41 waveform. Traditionally, such a source waveform is deterministically
 42 estimated from the field seismic data using well logs (e.g.,
 43 Edgar and van der Baan 2011). However, for shallow-water,
 44 very-high-resolution seismic reflection data, the source wave-
 45 forms are either intrinsically known (in the case of Chirp data;
 46 Gutowski *et al.* 2002) or can easily be derived from real, far-field
 47 measurements of the downgoing wavefield during static field
 48 trials (for Boomer and Sparker data). An advantage of the rel-
 49 atively short waveform periods of impulsive very-high-resolution
 50 sources (<2 ms for most Sparker and Boomer systems) is that
 51 only modest water depths (30–40 m) are required to get an
 52 uncontaminated, true far-field recording of the source waveform,
 53 while repeat measurements have shown these waveforms to be
 54

55 highly repeatable (Verbeek and McGee 1995; Muller *et al.*
 1 2 2002). This reduces the reliance on well logs, which in shallow
 3 water are commonly too short to get a reliable wavelet estimate,
 4 often resulting in phase mis-matches. The theoretical Sparker
 5 and Boomer wavelets used for the inversion examples shown in
 6 this paper were both derived from far-field measurements using
 7 a hydrophone suspended 30 m beneath the source.

8 In order to compare this synthetic trace with the field trace,
 9 both of these data require normalization against a reflector of
 10 known impedance contrast. With marine data this is commonly
 11 done using the seafloor reflection, which is strongest and the
 12 closest to being a true, near perfect white reflector, uncontami-
 13 nated by thin bed artefacts.

14 Data Preconditioning

15 Using a convolutional approach imposes a number of constraints
 16 on the form of the field seismic data being inverted. These take
 17 the form of three key assumptions: traces contain only normally
 18 incident, specularly reflected energy; no internal multiples are
 19 present; and the seismic wavelet is stationary.

20 The first assumption equates to either a subsurface consisting
 21 of horizontal, subparallel layering, or data that have been migrat-
 22 ed to geometrically correct for dipping structure and remove
 23 diffraction energy. For near-surface applications in actively
 24 depositing sedimentary basins, although the subsurface can be
 25 geometrically complex, velocity contrasts are generally small
 26 (often <<100 m/s). Meaning that, although migration is neces-
 27 sary to satisfy the assumptions of the convolutional model, time
 28 migration is normally adequate for geometrical correction, and
 29 where velocities are complex enough to warrant depth imaging
 30 (e.g., Biondi 2007; Morgan *et al.* 2011, 2013), the application of
 31 a 1D inversion approach would not be appropriately robust.

32 The lack of large velocity contrasts implies small reflection
 33 coefficients (generally <<1.0) in the shallow sub-surface, mean-
 34 ing that the effects of internal multiples are minimal. Traditional
 35 sea-surface multiple energy, however, is a common problem for
 36 shallow-water, very-high-resolution geophysical applications.
 37 The limited source-receiver offsets make multiple suppression
 38 difficult, while the shallow water depths mean the first multiple
 39 often overlaps real data. This is compounded by the short source
 40 wavelengths, which make reliable multiple prediction almost
 41 impossible due to subtle traveltime variations caused by sea state
 42 and changes in source/receiver depth. For these reasons, while
 43 internal multiples are unlikely to present a problem for the inver-
 44 sion process, the first multiple has to be taken as the maximum
 45 subsurface inversion depth attainable using this method.

46 The final assumption of a stationary seismic wavelet implies
 47 that trace amplitudes are not affected by wavefield spreading and
 48 attenuation. Most modern time migration algorithms are true
 49 amplitude (within the Born approximation), and therefore inher-
 50 ently correct for the spreading of energy across the wavefront
 51 (Bleistein 2001; Vardy and Henstock 2010). Attenuation,
 52 however, is more complex as this results in a loss of energy that

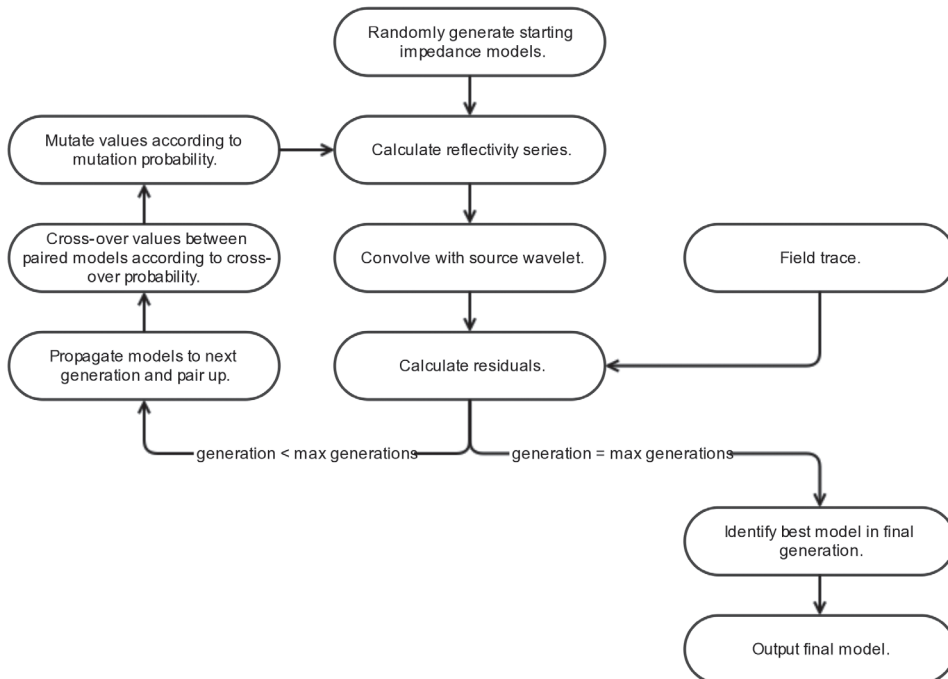


FIGURE 1
Flow chart showing basic processes of a genetic algorithm.

is not consistent across the source bandwidth, reducing reflector amplitudes and altering the seismic wavelet with depth. There are several published methods that invert high-resolution, near-surface seismic reflection data for Q_p , which is inversely proportional to the attenuation coefficient (α) (e.g., Schock *et al.* 1989; Stevenson *et al.* 2002; Pinson *et al.* 2008; Morgan *et al.* 2012). Using these techniques, estimates of the Q -factor can be made for sediments between the seafloor and multiple sub-seafloor reflectors (e.g., Vardy *et al.* 2012). This resulting subsurface Q -factor model can be used to approximate an amplitude correction according to the equation:

$$g(t) = e^{\alpha v(t)} \quad (2)$$

where $g(t)$ is the gain function, t the travel-time, and $v(t)$ the velocity.

For the examples presented in this paper, an attenuation correction has been estimated using equation 2. Alternatively, in areas where the subsurface is highly attenuating, the Q -factor model could be used to define a time-varying bandpass filter for application to synthetic traces during inversion. Applied using either a Short Time-window Fourier Transform (STFT) or a Wavelet Transform, such a filter would approximate the loss of higher frequencies at larger travel-times, thereby enabling a better fit between the field and synthetic seismic data.

Optimization Method

At the kernel of the inversion process is the optimization of an objective function. Commonly performed as a minimization of the residual between the field seismic data and the synthetic

trace, or the maximization of the cross-correlation between the two traces, such an optimization can be cast in two different ways. As a deterministic, iterative optimization of a linear or non-linear solver such as least-squares or conjugate gradient (e.g., Oldenburg *et al.* 1983). Or, alternatively, as a stochastic, global-search method such as simulated annealing (Sen and Stoffa 1991) or a genetic algorithm (e.g., Stoffa and Sen 1991; Sen and Stoffa 1992). Deterministic algorithms are simpler, but are prone to converging on local minima/maxima (normally a result of coherent noise) and produce a single, final impedance model with no statistically robust measure of accuracy beyond the fitness of the objective function (Sen and Stoffa 1996). In contrast, stochastic algorithms are more complex, but test a wider region of the parameter space, making them less sensitive to local minima/maxima in the objective function (Goldberg 1989). Stochastic-type algorithms also produce a family of models, each with a posteriori probability density function (PPD) that estimates the model likelihood in a statistically robust manner (Sen and Stoffa 1996).

To invert near-surface, shallow-water seismic data, a genetic algorithm (GA) (Goldberg 1989; Stoffa and Sen 1991) is used to minimize the residual between the field and synthetic seismic traces (Fig. 1). For a detailed description of mimicking the process of natural selection using a GA, the reader is directed to the seminal text of Goldberg (1989), while Stoffa and Sen (1991) describe in detail the specific application of a GA for the inversion of seismic reflection data.

For this application, the objective function is defined as:

$$E(m) = \sum_{j=1}^J |S_{field}^j - S_{synth}^j| \quad (3)$$

3 where $E(m)$ is the residual for model m , S_{field} and S_{synth} are the
4 field and synthetic trace amplitudes, and J the number of time
5 samples on each trace.

6 The ratio between the sum of all residuals for all models in
7 the current generation and the residual for each model is used to
8 define the likelihood PPD for each model within a generation:

$$9 L(m) = \frac{\sum_{n=1}^N E(n)}{E(m)} \quad (4)$$

10 where $L(m)$ is the likelihood of model m , $E(m)$ is the residual,
11 and N the number of models in the current generation.

12 This likelihood identifies the models with a better fitness that
13 should be propagated forward into the subsequent generation.
14 There are a number of selection mechanisms that define how this
15 subsequent generation should be populated (Sivaraj and
16 Ravichandran 2011), each striking a different balance between
17 convergence rate and a broad sampling of the parameter space. For
18 the application to near-surface, shallow-water seismic data, a
19 Stochastic Remainder sampling technique is used. Here, all models
20 with a better than average likelihood PPD are automatically
21 carried forward, while the remaining model spaces in the next
22 generation are populated at random. This ensures that models with
23 a better fitness are always maintained, allowing rapid convergence
24 when these models have a high degree of similarity. However, it
25 also ensures that a reasonable number of models with lower than
26 average likelihood PPD are carried forward, thereby maintaining
27 the dynamic range of parameter space being tested. This is particu-
28 larly important during early generations, where false positives can
29 easily produce a rapid convergence on a local minima.

32 CASE STUDY APPLICATION

33 To illustrate the use of a GA for impedance inversion of very-
34 high-resolution, shallow-water seismic reflection data, three
35 example profiles from the Sørfjorden side-fjord in northern
36 Norway are considered (L'Heureux *et al.* 2012; Vanneste *et al.*
37 2012; Vardy *et al.* 2012). These data consist of three coincident
38 Sparker, Boomer, and Chirp profiles running for c. 850 m in a
39 north-west to south-east direction (Figs 2 and 3). The Sparker and
40 Boomer profiles were acquired using a short multichannel
41 streamer (60 channels at 1 m group spacing), while the Chirp
42 profile is an arbitrary line extracted from a decimetre-resolution
43 3D seismic volume acquired using the 3D Chirp sub-bottom
44 profiler (Vardy *et al.* 2012).

45 To complement these seismic data, there is a significant record
46 of high-resolution geological (L'Heureux *et al.* 2012; Vanneste *et*
47 *al.* 2012) and geotechnical (Steiner *et al.* 2012) data for ground-
48 truthing. This includes over 20 short (<6 m) gravity cores, two
49 14-m long piston cores, 38 shorter (typically <5 m) free-fall cone-
50 penetrometer profiles (FF-CPTU), and one longer (24 m) pushed
51 cone penetrometer profile (CPTU). The profiles presented here
52 intersect with one piston core and four FF-CPTU locations. The
53 piston core has been processed using a multi-sensor core logger
54 (MSCL) for geological data and sampled for laboratory geotech-

5 nical tests, including Atterberg limits, fall cone strength, direct
6 simple shear, and triaxial testing (L'Heureux *et al.* 2012; Vanneste
7 *et al.* 2012). The FF-CPTU data have been processed to provide
8 pseudo-static soil mechanical properties, including undrained
9 shear-strength and density (Steiner *et al.* 2012).

10 Processing of the field seismic data prior to inversion fol-
11 lowed a simple workflow designed to improve signal-to-noise
12 and to geometrically correct while preserving the wavelet shape:

- 13 (i) Bandpass filtering to remove energy outside the known
14 source bandwidths using filter parameters of 0.2–0.3–5.0–
15 8.0 kHz for the Sparker and Boomer data. Energy outside the
16 source bandwidth had already been removed from the Chirp
17 data as part of the standard correlation with the known
18 source wavelet.
- 19 (ii) For the Sparker and Boomer data a predictive deconvolution
20 filter (operator = 6 ms; prediction = 1 ms) was applied to
21 reduce low frequency reverberation. This was not necessary
22 for the Chirp data.
- 23 (iii) Time migration using a slowly-varying RMS velocity model
24 constructed using reflector move-out analysis of the multi-
25 channel Sparker/Boomer data. For the Sparker and Boomer
26 data this was performed using a 2D pre-stack Kirchhoff time
27 migration in Landmark's Pro-MAX software, while the 3D
28 Chirp volume was 3D pre-stack Kirchhoff migrated using the
29 frequency-approximated algorithm of Vardy and Henstock
30 (2010). Time migrating these data improved the signal-to-
31 noise ratio and collapsed diffraction energy associated with
32 the polarity reversal to the south of the profiles.
- 33 (iv) Trace amplitudes were corrected for intrinsic attenuation
34 using equation 2, but a time-varying bandpass filter has not
35 been applied because attenuation is known to be low in the
36 very shallow interval of interest ($Q \geq 90$; Vardy *et al.* 2012).

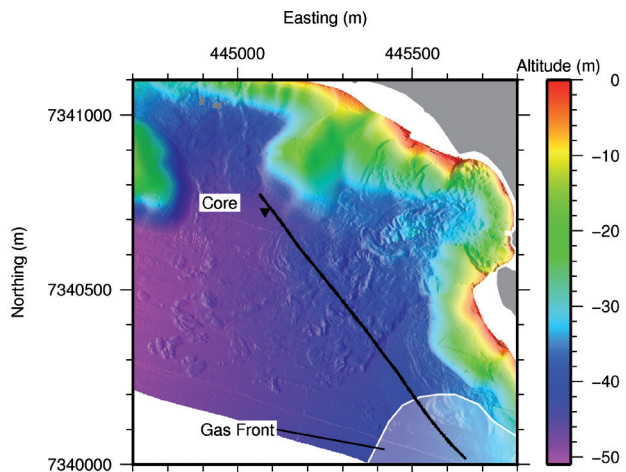


FIGURE 2

Location map showing seismic profiles (solid black line), core location (inverted black triangle), and shallow gas front (shaded white region) overlain on colour-shaded fjordbed bathymetric relief. Data are projected in UTM Zone 33N using the WGS1984 ellipsoid.

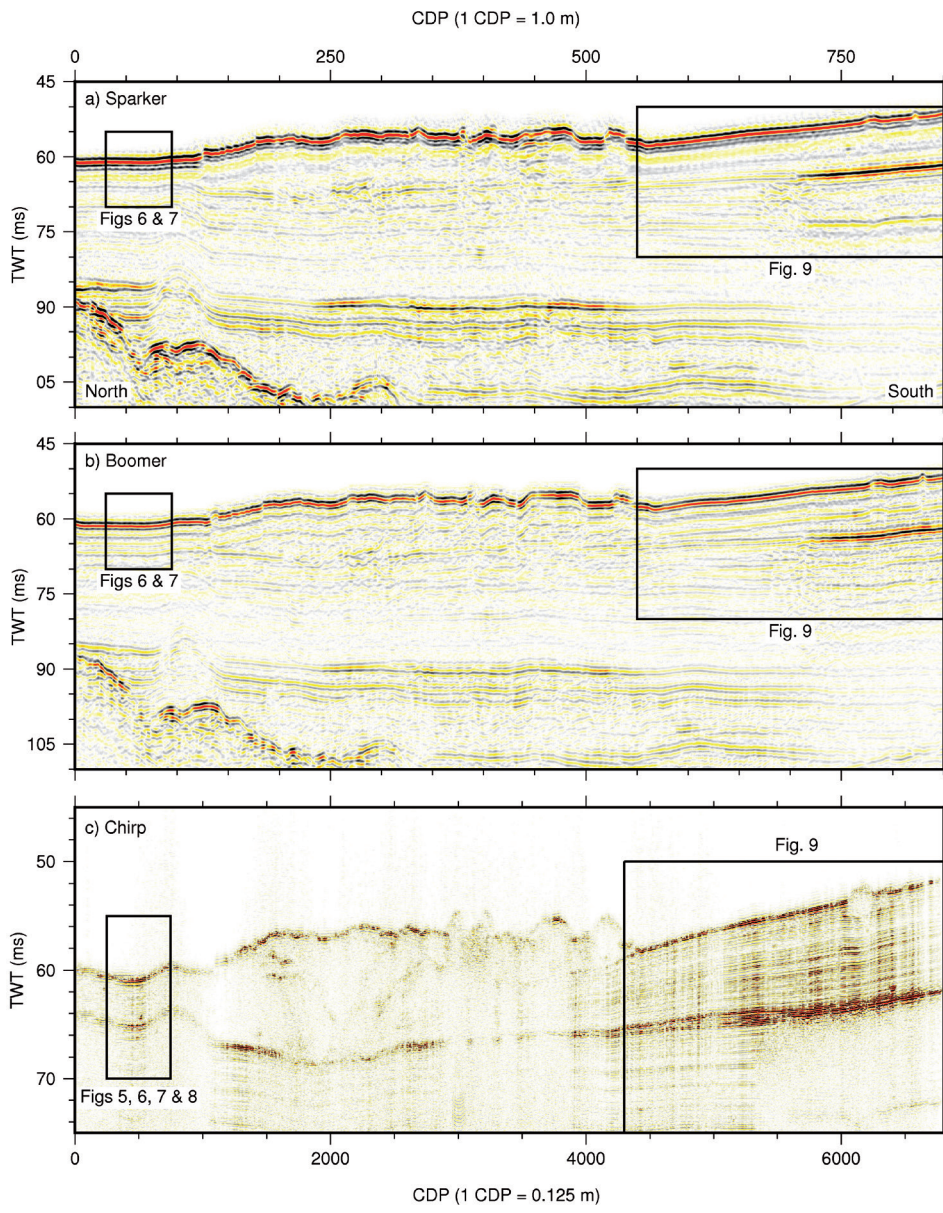


FIGURE 3

Three coincident very-high-resolution seismic reflection profiles acquired using Sparker (a), Boomer (b), and Chirp (c) sources. Note the expanded vertical scale on Chirp profile.

A major advantage of using a GA to optimize the objective function is that a starting model is not required; the initial generation of models being formed using impedances randomly generated within a specified range (Fig. 1). For the case study presented here, the impedances ranged between 1000 m/s g/cm³ (i.e., less than that of the water column; 1500 m/s g/cm³) and 3500 m/s g/cm³, which is significantly (>800 m/s g/cm³) larger than the maximum impedance recorded in the core data. Therefore, the presented impedance inversion results have not been artificially constrained by the initial conditions.

Subsequently, the inversion process is controlled by specifying the cross-over and mutation probabilities, as well as the number of models within each generation. The latter is important in ensuring the inversion samples a broad enough range of

parameter space, and therefore finds the global minimum, while the probabilities control the likelihood of a pair of impedance models swapping values and/or mutating to another random value in the next generation. Figures 4a through 4c illustrate the effect of varying these three parameters when inverting for the Chirp trace coincident with the core location (Fig. 5). Although these results vary from data set to data set, through testing on a range of data types from a variety of geographical locations it has heuristically been found that having more than 700 models per generation produces little appreciable improvement in optimization for a significantly increased computational cost (Fig. 4a). Similarly, cross-over and mutation probabilities of c. 0.6 and 0.2, respectively, appear to produce the optimum results (Figs 4b and c), but may need to be fine-tuned for each individual data set.

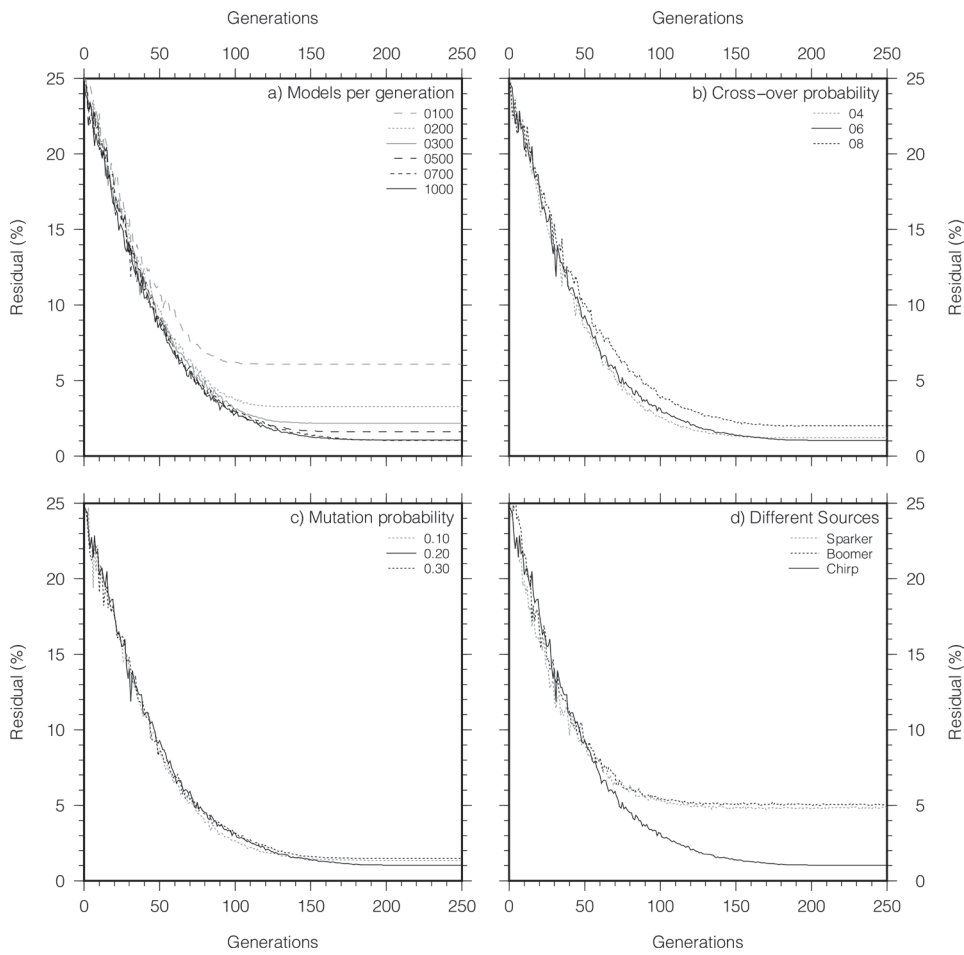


FIGURE 4

Evolution in residual of best model in each generation for Chirp trace coincident with core location while varying: number of models in each generation (a); cross-over probability (b); and mutation probability (c). Panel (d) shows optimum results for Sparker, Boomer and Chirp trace coincident with core location. Note, residual is plotted as average percentage error per sample.

RESULTS AND DISCUSSION

Inversion Results

Figure 5 shows inversion results from the core location at the northern end of the three seismic profiles. When compared to the Chirp field seismic data (Fig. 5a), the synthetic seismic section (Fig. 5b) demonstrates good reconstruction of several key reflections, most notably the strong seafloor return at c. 65 ms TWT and the composite reflector associated with landslide failure planes at c. 69 ms TWT. This similarity is shown more clearly through a wiggle trace comparison of coincident traces from the field (red line) and synthetic (black line) sections (Fig. 5d). The associated impedance section (Fig. 5c) demonstrates a sharp increase in acoustic impedance at the seafloor (1500 m/s g/cm^3 increasing to c. 2300 m/s g/cm^3) and a decrease in acoustic impedance associated with the composite reflector (by c. 500 m/s g/cm^3) at c. 69 ms TWT. There is only minor trace-to-trace variation, most likely a result of random noise contamination, but the overall impedance structure is highly consistent across the 32 m profile shown.

Comparison of a 1D impedance profile extracted from the core location demonstrates good correlation of structure with the MSCL impedance profile from the piston core (Fig. 5e). This relative impedance curve lacks the long wavelength consolidation

trend, but a subtle peak in impedance (c. 200 m/s g/cm^3 greater than background) at 68 ms TWT correlates well with the MSCL impedance profile, along with a significant decrease in impedance (up to 500 m/s g/cm^3) for the composite reflector at c. 69 ms TWT (Fig. 5e). The subtle increase at c. 68 ms TWT is well replicated in shape, but occurs c. 0.2 ms deeper in the core than the inverted profile. This offset is likely a result of core compression in the very shallow subsurface and serves to illustrate the difficulty in accurate vertical positioning of core structure in the top few metres.

The lack of replicating the consolidation trend is an inherent limitation of the impedance inversion technique. Casting the forward model as a convolution of the reflectivity series with a source waveform inherently limits the frequency of structure that can be reconstructed to the seismic bandwidth (1.5–13.0 kHz in the case of the Chirp data presented). In this case, the low frequency consolidation trend has to be estimated from core logged data (or well logs; Wagner *et al.* 2012). Figure 5f shows impedance profiles at the core site for Chirp, Boomer, and Sparker data that have been corrected to include the long wavelength consolidation estimated from the core log. Note that the Boomer and Sparker profiles are laterally offset to enable easier comparison. All three inverted profiles demonstrate very good replication of

the core impedance curve, albeit with different resolutions. The drop in impedance at c. 69 ms TWT is picked out in Boomer and Sparker inversions, but is less well constrained in time and appears as a broader drop in impedance demonstrating a contrast of only c. 300 m/s g/cm³ to background.

The effect of this can be seen in Fig. 4d, which plots the evolution of the residual for the best model for Sparker, Boomer, and Chirp traces coincident with the core location. The average residual per sample is c. 5% for the Boomer and Sparker data, whereas inversion of the Chirp data achieves a residual of c. 1%. Given the thin bed nature of this layer (c. 40 cm thick) relative to the Boomer and Sparker wavelengths (frequency bandwidth of 0.4–4.0 kHz equates to c. 3.75–0.38 m assuming 1500 m/s), this

is to be expected. Although it is still considered a thin bed for the first 2 octaves of the Chirp bandwidth (1.5–13.0 kHz equates to c. 1.00–0.12 m), the zero-phase nature of the Chirp wavelet simplifies the inversion as the relationship between peak energy and impedance contrast is significantly more stable in the presence of tuning (Widess 1973; Yilmaz 1987). In contrast, for the impulsive Sparker and Boomer sources, impedance contrasts normally correspond to the first zero-crossing, which is inherently unstable when wavelets begin to interact. The solution is non-unique and results in a significant number of local minima in parameter space, generally leading to an underestimate of the impedance contrast for such thin beds. The effect of this can be seen in Fig. 6, which shows the consolidation corrected impedance profiles for all three sources through the core site. The thin layer of low impedance is significantly better resolved in the Chirp profile (6a) than the Boomer and Sparker profiles (6b and c) where it is imaged as a broader and subtler decrease in impedance.

Figure 7 shows probability density distributions for the Chirp, Boomer, and Sparker impedance profiles from Fig. 5f, overlain by core derived impedance (white line). Warmer colours indicate a higher probability, while cooler colours indicate a lower probability. The results demonstrate both: the broad range of impedances tested for each time sample by the GA (see histograms extracted through low impedance thin bed at 69.2 ms TWT; Fig. 7d through f); and the high level of probability associated with the final impedance model (>0.65 in all cases). These results also demonstrate that the range of impedances with statistically meaningful probability is also relatively narrow for each time sample, in most case <100 m/s g/cm³ wide.

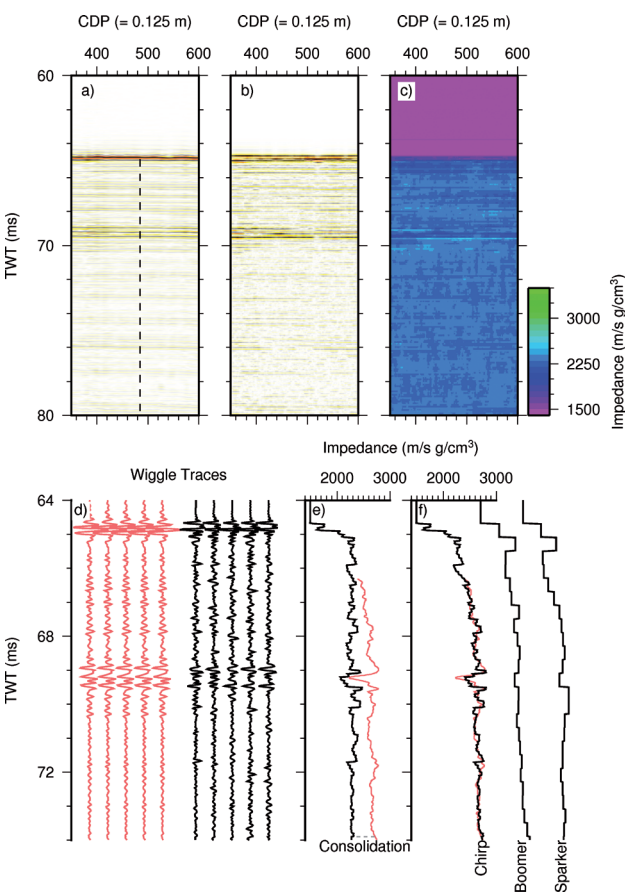


FIGURE 5

Field Chirp seismic section (a), synthetic seismic section (b), and impedance section (c) generated for a 32 m profile across the piston core location (vertical dashed line, panel a). Panel (d) compares synthetic (black line) and real (red line) traces extracted from the core location. Panel (e) shows 1D impedance profile from the synthetic data (black line) compared against the impedance profile from MSCL analysis of the core (red line), while panel (f) shows impedance profile corrected to include long wavelength consolidation trend for Chirp, Boomer, and Sparker data (black lines) together with core (red line). Note that in panel (f) the Boomer and Sparker profiles are laterally offset to allow for easier comparison.

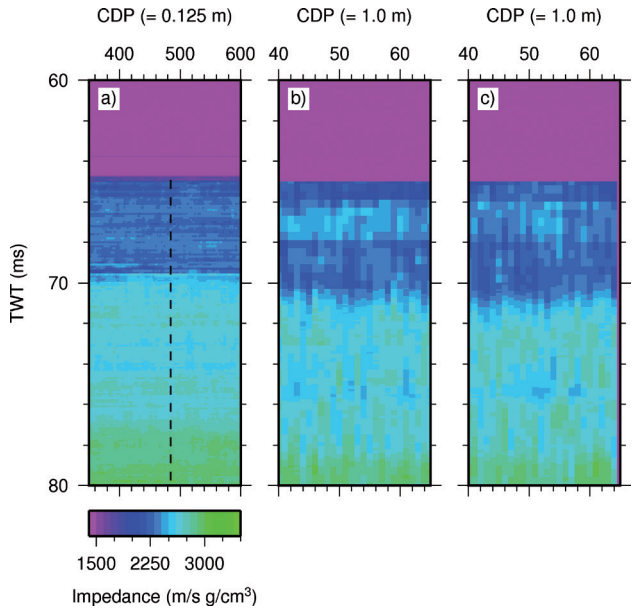


FIGURE 6

Panels (a) through (c) show 32 m long profile of acoustic impedance through the core site, generated using Chirp, Boomer, and Sparker data, respectively.

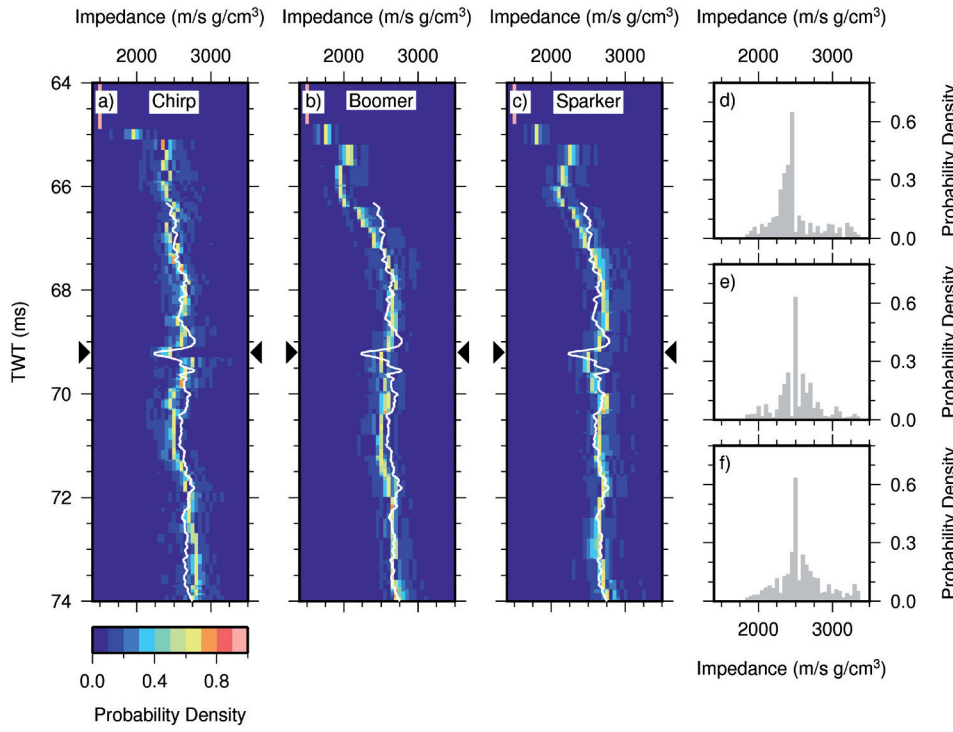


FIGURE 7

Panels (a) through (c) show probability densities binned at 50 m/s g/cm^3 intervals for the Chirp, Boomer, and Sparker impedance profiles shown in Fig. 5e. Impedances coloured deep blue have a very low probability, while those coloured warmer orange and red have high probabilities. White line overlay shows impedance profile from MSCL core analysis. Panels (d) through (f) show histograms of the probability density for each source extracted through the peak of the low impedance layer at 69.2 ms TWT.

Soil Properties Interpretation

Although inverting very-high-resolution seismic reflection data to produce 2D acoustic impedance profiles, such as shown in Fig. 6, provides a useful step beyond traditional structural mapping, acoustic impedance is not the most intuitive quantitative property for interpreting the nature of the subsurface. Figure 8a through d shows cross-plots of acoustic impedance against four key physical properties (P-wave velocity, density, mean grain size, and porosity) using data derived from the literature (Shumway 1960; Hamilton 1972; Richardson and Briggs 2004; Kraft *et al.* 2005). Black symbols represent data derived either *in situ* or using resonance column testing at seismic frequencies and *in situ* pressures (Shumway 1960; Hamilton 1972), whereas solid grey symbols are data derived at higher frequencies than those typically produced by very-high-resolution seismic sources and not at *in situ* pressures (Richardson and Briggs 2004; Kraft *et al.* 2005). Data acquired at higher frequencies than the seismic sources (typically c. 500 kHz as opposed to 0.4–24.0 kHz) are susceptible to frequency-dependent dispersion, and may not therefore be an accurate representation of the relationship between the soils and the acoustic wavefield at seismic frequencies (see, Buckingham 2000). Similarly, the high porosity, unconsolidated nature of shallow subsurface sediments mean that MSCL measurements made on cores in the laboratory at atmospheric pressure rather than *in situ* pressure are likely to differ due to dewatering and consolidation.

Empirical relationships between physical properties and impedance (dashed grey lines Fig. 8 and Table 1) were derived using a weighted regression, with greater weight applied to the

data derived at seismic frequencies (Shumway 1960; Hamilton 1972). Using these relationships, the inverted impedance profiles can be related to P-wave velocity, density, mean grain size, and porosity. Figure 8e shows the Chirp profile from the core location (Fig. 5f) converted into soil properties and plotted against appropriate core logs.

The mean grain size agrees well with core lithologies, in which the subsurface is identified as predominantly silty (5–6 ϕ), while the thin bed correlating with the composite reflector is two 10–15 cm thick clay-rich layers sandwiching a 5 cm thick sand seam (L'Heureux *et al.* 2012). In the impedance derived mean grain size, this layer is clearly highlighted as a 40–50 cm thick bed c. one ϕ finer than the background sediments. The inverted porosity shows matching structure to the core-derived porosity measurements, but is systematically 15–20% higher. This is likely a result of core dewatering and demonstrates the potentially significant underestimate possible when logging porosity or water content from core samples. Similarly, the P-wave velocity profile demonstrates good agreement between the synthetic and MSCL profiles, but the MSCL data appears systematically offset by c. –20 m/s. The density, however, demonstrates an excellent agreement in both shape and magnitude, with a maximum offset of < 0.1 g/cm^3 .

Deriving such soil properties using inversion techniques permits these properties to be mapped spatially, no longer being constrained to 1D core localities. At the southern end of the profiles, the clay-rich composite bed demonstrates a clear polarity reversal and significant strengthening in amplitude (greater than an order of magnitude; Fig. 3). By inverting along the entire

length of the seismic profiles, this polarity reversal is observed to correspond with a laterally confined thin lens of low acoustic impedance, c. 1000 m/s g/cm³ less than the background matrix (Fig. 9). Using the empirical relationships from Table 1, this drop in acoustic impedance can be related to a change in P-wave velocity of at least –100 m/s relative to the background sediment clearly imaged on all three seismic profiles (Figs 9d through f). While in the inverted Sparker and Boomer profiles the velocity anomaly is imaged as a continuous lens of lower velocities (50–100 m/s below background), the higher resolution Chirp profile appears to indicate a more patchy distribution, with localised, larger velocity anomalies up to 150 m/s below the background

(Fig. 9f). Such polarity-reversed reflections are normally indicative of shallow gas (Missiaen *et al.* 2002), and the observed velocity anomaly would be consistent with a thin lens of (probably biogenically derived) shallow gas trapped in the finer grained layer coincident with the failure planes for multiple regional landslides.

This is consistent with the patchiness of the higher resolution Chirp inversion (12.5 cm trace spacing and c. 10 cm, vertical resolution) as well as the work of Morgan *et al.* (2012), who invert for gas saturation from Q-factor using airgun data, obtaining gas saturation estimates between 0.10 % and 0.20 %. Such gas saturation values are too low to affect the mechanical

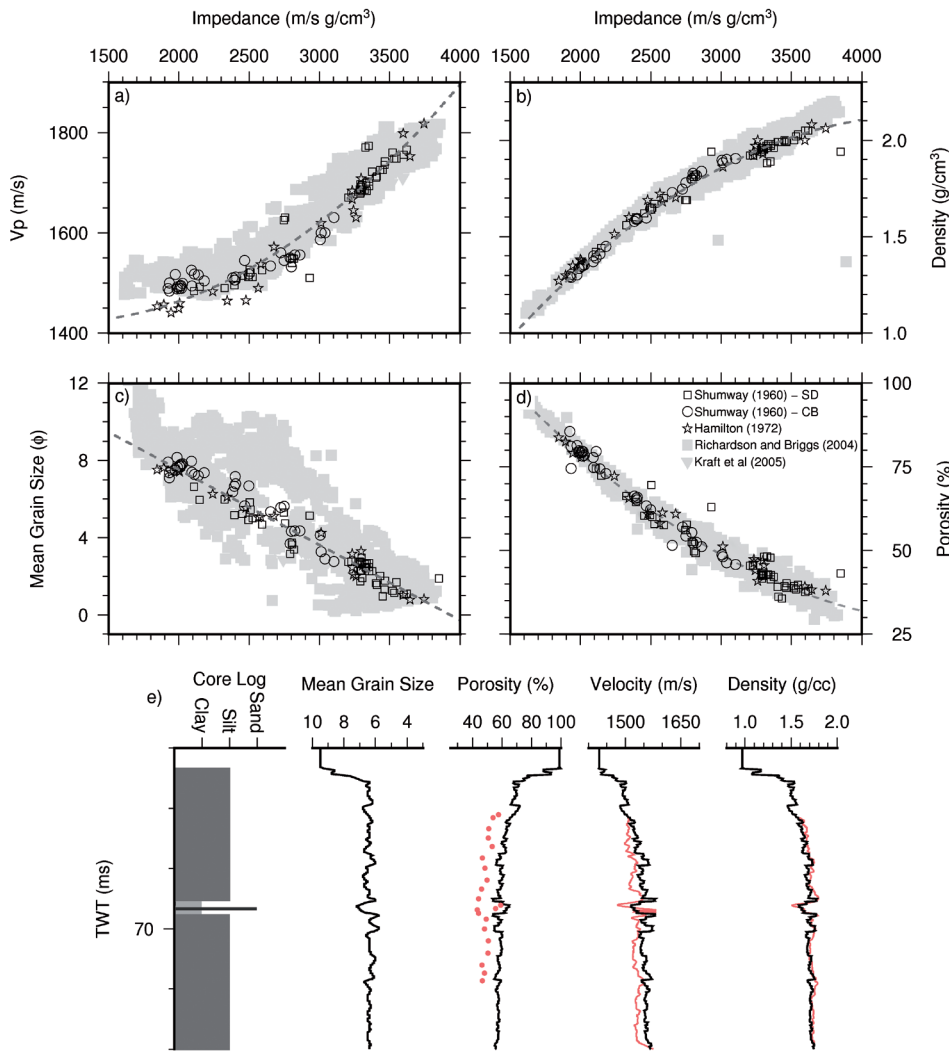


FIGURE 8

Panels (a) through (d) are cross-plots of acoustic impedance against four remote physical properties (P-wave velocity, density, mean grain size, and porosity) collated from the literature (Shumway 1960; Hamilton 1972; Richardson and Briggs 2004; Kraft *et al.* 2005). Black symbols indicate *in situ* or resonance column measurements made at seismic frequencies, while grey symbols indicate data acquired at higher frequencies (300–500 kHz). Dashed grey lines are weighted best-fit relationships using the equations from Table 1. Panel (e) plots remote physical properties derived from these relationships applied to the Chirp impedance profile from Fig. 5 against core derived data.

Property	Equation	R ²
P-wave velocity (m/s)	1500 - 0.13549Z + 0.0000586Z ²	0.94
Density (g/cc)	-0.52 + 0.0012Z - 0.000000136Z ²	0.99
Mean Grain Size (φ)	15.32 + 0.0039Z	0.97
Porosity (%)	178.6 - 0.06307Z + 0.000006604Z ²	0.99

TABLE 1

Relationship between acoustic impedance (Z) and remote sediment properties derived using weighted regression of data shown in Fig. 8.

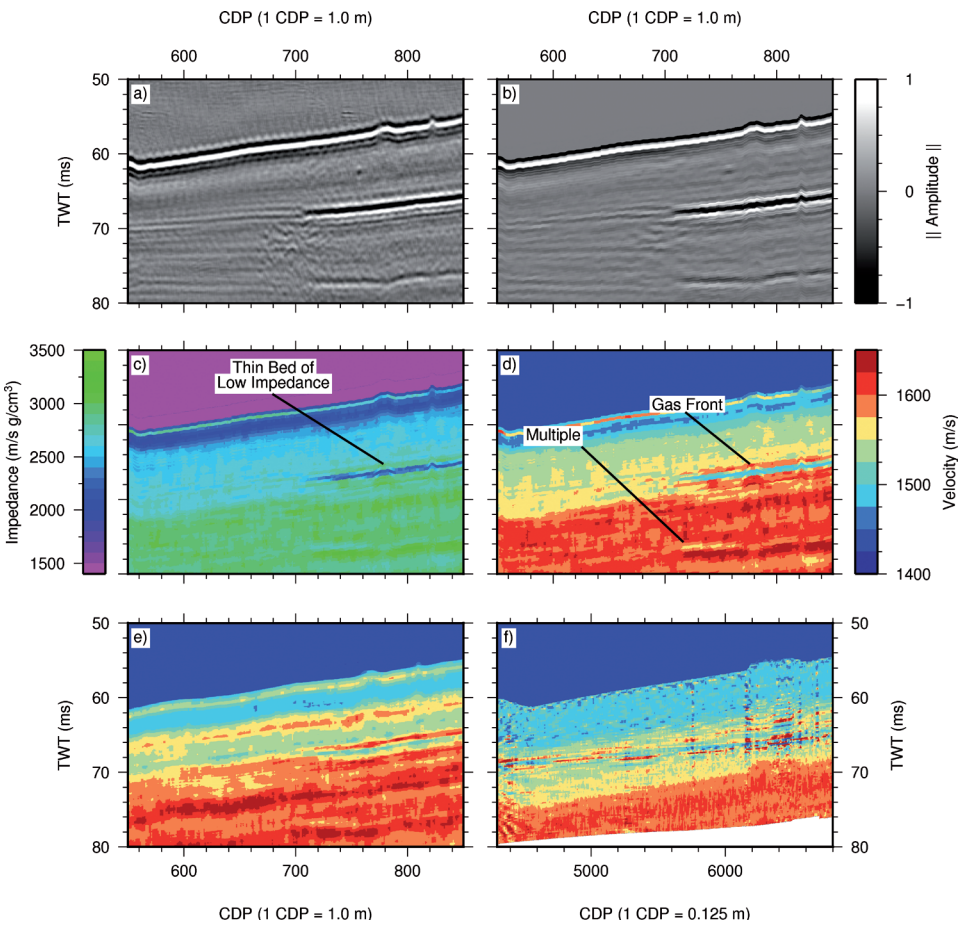


FIGURE 9

Field Sparker seismic section (a), synthetic seismic section (b) and accompanying impedance section (c) generated for the southern end of the profile (see, Fig. 3). Panel (c) shows a thin bed of low acoustic impedance coincident with the high amplitude, polarity reversed reflection. Panels (d) through (f) show P-wave velocity profiles calculated for Sparker, Boomer, and Chirp profiles using empirical relationship given in Table 1.

strength of the soils, indicating that this method is sensitive enough to provide meaningful geotechnical information.

CONCLUSIONS

The work presented demonstrates the potential of applying post-stack acoustic impedance inversion to very-high-resolution marine seismic reflection data. The composite reflector that corresponds to the failure plane depth for multiple local landslides was distinguished as a thin bed of low acoustic impedance clearly identified in inverted Chirp, Boomer, and Sparker profiles (despite being <50 cm thick). Use of empirical relationships between acoustic impedance and remote sediment properties indicates this layer has a smaller mean grain size (by at least one ϕ) and a lower bulk density (by c. 0.2 g/cm³) than the background sediment, which is consistent with laboratory core analysis. Additionally, where the polarity reverses to the southern end of all three lines, the inversion results indicate a thin lens of shallow gas (velocity contrast at least -100 m/s) that is consistent with previously published results (Morgan *et al.* 2012).

These results imply that, not only is it possible to invert very-high-resolution marine seismic reflection data for remote sediment properties, but it can also be done with a sensitivity to the sediment properties that provides useful *in situ* geological and

geotechnical information. Successful discrimination of a complex clay-rich thin bed within a silty-clay background matrix, and a well defined P-wave velocity anomaly when gas saturation levels are below the threshold where the mechanical strength of the soils is influenced, demonstrate the potential of this technique for providing high fidelity sediment property information. Here I have presented results from a slope stability application, but this technique has the potential to be of use for a range of shallow-water problems.

ACKNOWLEDGMENTS

The author wishes to thank Maarten Vanneste, Jean-Sebastien L'Heureux, Oddvar Longva, Shyam Chand, John Anders Dhal, and John Davis for their help in acquiring the data used as the field data case study, along with Tim Henstock, Isabelle Lecomte and Hector Marin Moreno for their informative discussions regarding inversion. Additionally the author would like to acknowledge the comments of two anonymous reviewers, which significantly improved the manuscript. The field data preconditioning was performed using Landmark's ProMAX software. All other processing used custom algorithms, including the genetic algorithm for inversion. This is paper no. 433 for the International Centre for Geohazards.

3
4
5
6
7
8
9
10
11
12
13
14
15
16
17
18
19
20
21
22
23
24
25
26
27
28
29
30
31
32
33
34
35
36
37
38
39
40
41
42
43
44
45
46
47
48
49
50
51
52
53
54
55
REFERENCES

- Biondi B. 2007. Concepts and Applications in 3D Seismic Imaging. In: *SEG Distinguished Instructor Short Course 10*, SEG, Tulsa, Oklahoma, USA.
- Bleistein N. 2001. *Mathematics of Multidimensional Seismic Imaging, Migration, and Inversion*. Springer-Verlag, Inc.
- Bosch M., Mukerji T. and Gonzalez E. 2010. Seismic inversion for reservoir properties combining statistical rock physics and geostatistics: a review. *Geophysics* **75**, A165–A176.
- Buckingham M. 2000. Wave propagation, stress relaxation, and grain-to-grain shearing in saturated, unconsolidated marine sediments. *Journal of the Acoustics Society of America* **108**, 2796–2815.
- Bull J.M., Quinn R. and Dix J. 1998. Reflection coefficient calculation from marine high-resolution seismic reflection (Chirp) data and application to an archaeological case study. *Marine Geophysical Researches* **20**, 1–11.
- Cooke D.A. and Schneider W.A. 1983. Generalized linear inversion of reflection seismic data. *Geophysics*, **48**(6), 665–676.
- Edgar J. And van der Baan M. 2011. How reliable is statistical wavelet estimation? *Geophysics* **76**(4), V59–V68.
- Goldberg D. 1989. *Genetic Algorithms in Search, Optimization, and Machine Learning*, Addison Wesley Publishing Company, Reading, MA.
- Gutowski M., Bull J.M., Dix J., Henstock T., Hogarth P., White P. and Leighton T. 2002. Chirp sub-bottom profiler source signature design and field testing. *Marine Geophysical Researches* **23**, 481–492.
- Gutowski M., Bull J.M., Dix J., Henstock T.J., Hogarth P., Hiller T., Leighton T. and White P. 2008. 3D high-resolution acoustic imaging of the sub-seabed. *Applied Acoustics* **69**(5), 412–421.
- Hamilton E. 1972. Compressional Wave Attenuation in Marine Sediments. *Geophysics* **37**(4), 620–646.
- Kraft B., Ressler J., Mayer L., Fonseca L. and McGillicuddy G. 2005. In-situ measurement of sediment acoustic properties. In: *Proceedings of the International Conference Underwater Acoustic Measurements: Technologies and Results*, Acoustical Society of America.
- L'Heureux J.-S., Longva O., Steiner A., Hansen L., Vardy M., Vanneste M. et al. 2012. Identification of Weak Layers and Their Role for the Stability of Slopes at Finneid fjord, Northern Norway. In: *Submarine Mass Movements and Their Consequences 31*, Advances in Natural and Technological Hazards Research, pp. 321–330, Springer, Heidelberg, DE.
- Mallick S. 2001. Prestack waveform inversion using a genetic algorithm – The present and the future. *CSEG Recorder* **26**(6), 78–84.
- Missiaen T., Murphy S., Loncke L. and Henriet J.-P. 2002. Very high-resolution seismic mapping of shallow gas in the Belgian coastal zone. *Continental Shelf Research* **22**, 2291–2301.
- Morgan E., Vanneste M., Lecomte I., Baise L., Longva O. and McAdoo B. 2012. Estimation of free gas saturation from seismic reflection surveys by the genetic algorithm inversion of a P-wave attenuation model. *Geophysics* **77**(4), R175–R187.
- Morgan J., Warner M., Collins G., Grieve R., Christeson G., Gulick S. et al. 2011. Full waveform tomographic images of the peak ring at the Chicxulub impact crater. *Journal of Geophysical Research* **116**, B06303.
- Morgan J., Warner M., Bell R., Ashley J., Barnes D., Little R., Roele K. and Jones C. 2013. Next-generation seismic experiments: wide-angle, multi-azimuth, three-dimensional, full-waveform inversion. *Geophysical Journal International* **195**, 1657–1678.
- Mueller C., Woelz S. and Kalmar S. 2013. High-Resolution 3D Marine Seismic Investigation of Hedeby Harbour, Germany. *The International Journal of Nautical Archaeology* **42**(2), 326–336.
- Muller C., Mikereit B., Bohlen T. and Theilen F. 2002. Towards high-resolution 3D marine seismic surveying using Boomer sources. *Geophysical Prospecting* **50**, 517–526.
- Muller C., Woelz S., Ersoy Y., Boyce J., Jokisch T., Wendt G. and Rabbel W. 2009. Ultra-high-resolution marine 2D-3D seismic investigation of the Liman Tepe/Karatina Island archaeological site (Urla/Turkey). *Journal of Applied Geophysics* **68**, 124–134.
- Oldenburg D., Scheuer T. and Levy S. 1983. Recovery of the acoustic impedance from reflection seismograms. *Geophysics* **48**, 1318–1337.
- Palamenghi L., Schwenk T., Spiess V. and Kudrass H. 2011. Seismostratigraphic analysis with centennial to decadal time resolution of the sediment sink in the Ganges–Brahmaputra subaqueous delta. *Continental Shelf Research* **31**(6), 712–730.
- Panda S., LeBlanc L. and Schock S. 1994. Sediment classification based on impedance and attenuation estimation. *J. Acoustic. Soc. Amer.* **96**(5), 3022–3035.
- Pinson L., Henstock T., Dix J. and Bull J. 2008. Estimating quality factor and mean grain size of sediments from high-resolution marine seismic data. *Geophysics* **73**(4), G19–G28.
- Pinson L., Vardy M., Dix J., Henstock T., Bull J. and MacLachlan S. 2013. Deglacial history of glacial lake Windermere, UK; implications for the central British and Irish Ice Sheet. *Journal of Quaternary Science* **28**(1), 83–94.
- Plets R., Dix J., Adams J. and Best A. 2008. 3D Reconstruction of a Shallow Archaeological Site from High-Resolution Acoustic Imagery: the Grace Dieu. *Applied Acoustics* **69**, 399–411.
- Richardson M. and Briggs K. 2004. Empirical Predictions of Seafloor Properties Based on Remotely Measured Sediment Impedance. In: *High Frequency Ocean Acoustics Conference*, pp. 12–21, AIP, Melville, NY.
- Schock S., LeBlanc L. and Mayer L. 1989. Chirp subbottom profiler for quantitative sediment analysis. *Geophysics* **54**(4), 445–450.
- Schock S., Tellier A., Wulf J., Sara J. and Erickson M. 2001. Buried object scanning sonar. *IEEE Journal of Ocean Engineering* **26**(4), 677–689.
- Sen M. and Stoffa P. 1991. Nonlinear one dimensional seismic waveform inversion using simulated annealing. *Geophysics* **56**(10), 1624–1638.
- Sen M. and Stoffa P. 1992. Rapid sampling of model space using genetic algorithms: Examples from seismic waveform inversion. *Geophysical Journal International* **108**, 281–292.
- Sen M. and Stoffa P. 1996. Bayesian inference, Gibb's sampler and uncertainty estimation in geophysical inversion. *Geophysical Prospecting* **44**, 313–350.
- Sheriff R. 2002. Encyclopedic Dictionary of Applied Geophysics. In: *Geophysical Reference Series 13*, SEG, 4th edn.
- Shumway G. 1960. Sound speed and absorption studies of marine sediments by a resonance method. *Geophysics* **25**(2), 451–467.
- Sivaraj R. and Ravichandran T. 2011. A review of selection methods in Genetic Algorithms. *International Journal of Engineering Science and Technology* **3**(5), 3792–3797.
- Steiner A., L'Heureux J.-S., Kopf A., Vanneste M., Longva O., Lange M. et al. 2012. An In-Situ Free-Fall Piezocone Penetrometer for Characterizing Soft and Sensitive Clays at Finneid fjord (Northern Norway). In: *Submarine Mass Movements and Their Consequences*, vol. 31 of Advances in Natural and Technological Hazards Research, pp. 99–109, Springer, Heidelberg, DE.
- Stevenson I., McCann C. and Runciman P. 2002. An attenuation-based sediment classification technique using Chirp sub-bottom profiler data and laboratory acoustic analysis. *Marine Geophysical Researches* **23**, 277–298.
- Stoffa P. and Sen M. 1991. Nonlinear multiparameter optimization using genetic algorithms: inversion of plane wave seismograms. *Geophysics* **56**(11), 1794–1810.
- Stoker M., Bradwell T., Howe J., Wilkinson I. and McIntyre K. 2009. Lateglacial ice-cap dynamics in NW Scotland: evidence from the

- fjords of the Summer Isles region. *Quaternary Science Reviews* **28**, 3161–3184.
- Vanneste M., L'Heureux J.-S., Brendryen J., Baeten N., Larberg J., Vardy M. *et al.* 2012. Assessing offshore geohazards: A multi-disciplinary research initiative to understand shallow landslides and their dynamics in coastal and deepwater environments, Norway. In: *Submarine Mass Movements and Their Consequences*, vol. 31 of Advances in Natural and Technological Hazards Research, pp. 29–41, Springer, Heidelberg, DE.
- Vardy M. and Henstock T. 2010. A frequency approximated approach to Kirchhoff migration. *Geophysics* **75**(6), S211–S218.
- Vardy M., Dix J., Henstock T., Bull J. and Gutowski M. 2008. Decimetre-resolution 3D seismic volume in shallow water; a case study in small object detection. *Geophysics* **73**(2), B33–B40.
- Vardy M., Pinson L., Bull J., Dix J., Henstock T., Davis J. and Gutowski M. 2010. 3D seismic imaging of buried Younger Dryas mass movement flows: Lake Windermere, UK. *Geomorphology* **118**, 176–187.
- Vardy M., L'Heureux J.-S., Vanneste M., Longva O., Steiner A., Forsberg C. *et al.* 2012. Multidisciplinary investigation of a shallow near-shore landslide, Finneidfjord, Norway. *Near Surface Geophysics* **10**, 267–277.
- Verbeek N. and McGee T. 1995. Characteristics of high-resolution marine reflection profiling sources. *Journal of Applied Geophysics* **33**, 251–269.
- Wagner C., Gonzalez A., Agarwal V., Koesoemadinata A., Ng D., Trares S., Biles N. and Fisher K. 2012. Quantitative application of poststack acoustic impedance inversion to subsalt reservoir development. *The Leading Edge* **31**, 528–537.
- Wardell N., Diviacco P. and Sinceri R. 2002. 3D pre-processing techniques for marine VHR seismic data. *First Break* **20**(7).
- Widess M.B. 1973. How Thin is a Thin Bed? *Geophysics* **6**, 1176–1180.
- Yilmaz O. 1987. *Seismic Data Processing*, vol. 2 of *Investigations in Geophysics*, SEG, Tulsa, USA, 1st ed.